eJSE International

Special Issue: Electronic Journal of Structural Engineering 13(1) 2013

Determination of dynamic ballast characteristics under transient impact loading

Akira AIKAWA

Railway Dynamics Division, Railway Technical Research Institute, Tokyo, Japan

Email: aikawa.akira.11@rtri.or.jp

ABSTRACT: Train-related impact loads acting on a sleeper bottom were directly measured and spectral analysis was performed to determine the dynamic characteristics of ballast layer under traffic impact loads. The results indicate that broadband vibration components act on the ballast layer, which exhibits two different types of behavior depending on dynamic stiffness characteristics. For vibration components over 100 Hz, the layer has high rigidity, resists dynamic loading sufficiently and absorbs impact loading adequately. However, in the low-frequency range, it easily deforms and is hard to absorb load components. FE vibration analysis of ballast aggregate was also performed to examine related characteristics. The mechanisms by which wave propagation velocity inside a ballast layer is reduced and wave motion inside it is greatly reduced were numerically simulated using only elastic body analysis without consideration of material nonlinearity.

Keywords: Ballasted track, Field measurement, Concrete sleeper, Spectral analysis, Finite element analysis

1 INTRODUCTION

Ballast piece abrasion, breakage and movement are major influences in ballast degradation, which is related to impact loads originating at the interface between rails and the wheels of passing trains. Each of these influences induces two different types of motion within the ballast layer. One is displacement in the low-frequency domain due to rigid-body motion, which is characterized by the low-frequency bounce mode determined from body weight and ballast elasticity (originally caused by deflection motion occurring when a heavy axle passes over the rail). The other is elastic vibration in the high-frequency domain, which is generated by elastic wave propagation inside ballast solids (originally caused by impulse waves generated from the mechanism of rolling contact between wheels and rails).

By applying loads of high-speed trains via hydraulic jacks to a reduced-scale ballast model with three sleepers, Shaer et al. simulated the dynamic behavior of ballasted track with high-speed train operation, and Schmitt et al. numerically simulated the related phenomena. The results of these experiments show that the extent of settlement depends strongly on the velocity of the train applying the load, and that the settlement rate is very high when acceleration exceeds a certain critical value. In contrast to the outcomes of previous research, the subsidence curve determined in this work shows a discontinuous stepped function. Azema et al. numerically investigated granular materials composed of irregular polyhedral ballast pieces and evaluated the force transmission and fabric properties of a mixture of irregularly shaped ballast pieces. Kaewunruen and Remennikov investigated the vibration characteristics of sleepers and studied the influence of asymmetrical wheel loading on sleepers in reference to sleeper bending behavior. Indraratna et al. and Lackenby et al. demonstrated that most ballast degradation is primarily attributable to edge chipping rather than full splitting, and Aursudkij observed similar results in a test facility. Lu and McDowell also found that most ballast degradation is primarily attributable to edge chipping. Conventional railway ballast vibration measurement techniques based on the use of uniaxial accelerating sensors have been widely employed to elucidate ballast stone behavior, and methods involving the use of triaxial accelerating sensors have also been adopted. However, the dynamic characteristics of ballast layers in relation to repeated impact loads have not yet been sufficiently elucidated, and their clarification is expected

to contribute to a fuller understanding of ballast degradation phenomena.

To determine the characteristics of dynamic load transfer at contact points within the boundary layer between sleepers and ballast, a special sensing sleeper fitted with a large number of thin impact force sensors attached to its whole undersurface was developed. This paper details the related principles and describes field experiments performed to determine the applicability of the method. After its suitability was confirmed, measurements were taken for over a month to clarify the characteristics of impact load transmission within the ballast layer. Spectral analysis enabled evaluation of ballast layer dynamic characteristics, especially in terms of their dependence on frequency. Next, the paper describes newly developed techniques for use in three-dimensional dynamic numerical model studies of ballasted railway track. The results obtained from the technique were used to evaluate the dynamic behavior of ballast aggregate and to elucidate impact-load-induced wave propagation inside ballast pieces.

2 MEASUREMENT SPECIFICATIONS

2.1 Development of ultra-thin impact force sensors

From among the various types of load sensors available, a sheet-type impact force model was adopted for this study (Figure 1) in consideration of its capacity to measure the total force acting on a plane, forces of up to 10 kN over an area measuring 64 cm^2 and dynamic loads on components from 0.01 Hz up to 50 kHz, and for its thickness of 2 cm or less, enabling attachment to the sleeper undersurface.

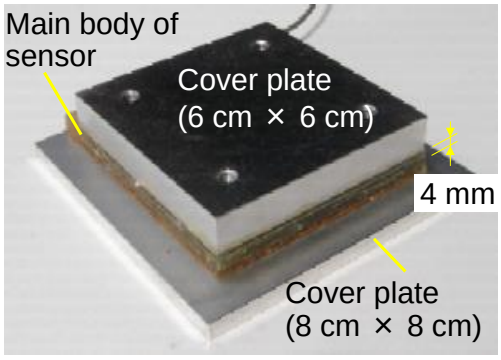

Figure 1: Ultra-thin impact force sensor made using piezoelectric film

Each sensor has a main body and cover members. The main body, measuring 6 cm in width and length and 4 mm in thickness, is made from piezoelectric film sheet and silicone rubber, and has metal plates on both surfaces. It is electrically equivalent to a capacitor, therefore, the sensor has no internal resistance, and no noise is generated by induced currents. In addition, the film produces a relatively large charge corresponding to voltage (in the region of several tens of volts) in proportion to mechanical impact loads and it has a favorable S/N ratio. Accordingly, it does not need a low-pass filter. Data obtained from on-site measurement indicate that the magnitude of noise is 0.003% or less for the largest load measurable.

The cover members are solid high-strength aluminum alloy cover plates on the front, measuring 8 cm in width and length and 5 mm in thickness, and back, measuring 6 cm in width and length and 1 cm in thickness, of the sensor. The front plate transmits impact loads to the main body and prevents breakage of the sensor itself as a result of impact loads from running trains. The back plate, which has a screw hole in each of its four corners, is used to fix the sensor firmly to the sleeper. A 2 cm wide space in the back of the front plate is provided for wiring with complete shielding to eliminate noise problems induced by train driving power. The performance of all impact force sensors was examined in a loading test using an impulse hammer (5 kN maximum load), and a calibration value was calculated for each one.

2.2 Design and fabrication of a thin concrete mono-block sleeper

Figure 2 shows an overview of the sensing-sleeper measurement equipment designed to support the assessment of dynamic load distribution on the sleeper undersurface at high frequencies of up to several thousand Hertz. The sleeper has the same size and shape as the PC3-type mono-block concrete sleeper most commonly employed on conventional ballasted tracks in Japan.

Figure 2: Overview of sensing sleeper

Although the 2 cm thick impact force sensors attached to the undersurface of the sleeper are thinner than the conventional type force sensors, a sleeper with a level of sensitivity comparable to that

achieved with conventional products was designed and manufactured as shown in Figure 3. The sleeper's strength performance levels were confirmed in a static force resistance test. A total of 75 impact force sensors were attached with no mutual clearance to the whole undersurface in a 25 times 3 matrix arrangement to form a solid structure. The sensors were precisely fixed in position on a 5 mm thick metal unit board corresponding to the sleeper undersurface size, and the board was then attached to the sleeper undersurface. The sleeper's sensory and safety performance levels were also confirmed beforehand in an insulation resistance test, a laboratory strength test (Japanese Standards Association, 2002) and a running experiment on a test railway track.

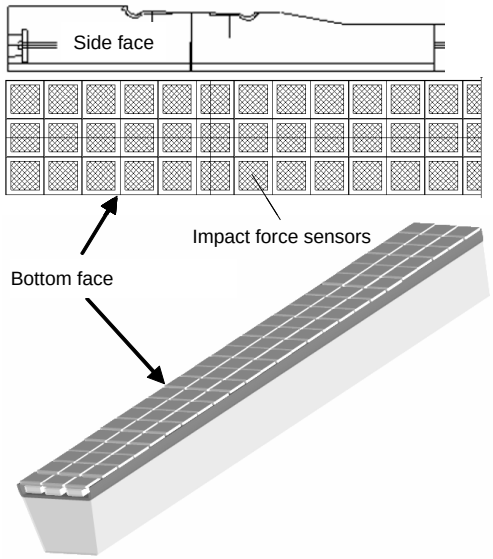

Figure 3: Design and fabrication of thin PC3-type concrete sleeper

2.3 Active integrated circuit

The sensor consists of thin metal plates attached to both sides of a thin piezo film, giving the same structure as an electric-circuit condenser. As there is no internal resistance structure, no current induced by noise sources occurs even in the high-tension environments of train operation, thereby enabling high-quality load measurement. Although a charge proportional to impact loading is output from both terminals, it is extremely difficult to digitize the charge output. Accordingly, the charge from the sensor is usually converted into a voltage using an integration circuit attached to a sensor output terminal (a charge amp). A setup such as an impedance transformation circuit with a high-impedance operational amplifier is sufficient for this purpose.

As the sensor also demonstrates favorable reactivity and output voltage as large as several tens of volts, a passive integration circuit consisting of one film-type condenser (4.4 μF) using no utility power is suitable for operation. Although this type of circuit cannot be used to measure direct current components, its linearity in the 0.1 Hz to 10 kHz frequency range was confirmed by numerical simulation using an equivalent circuit and in laboratory dynamic loading testing. This arrangement is considered to offer sufficient performance to enable track measurement.

According to the outcomes of a measurement experiment on a Railway Technical Research Institute test railway line, the influence of phase delay in a passive-type integration circuit is non-negligible in the very low-frequency range. By introducing an impedance transformation preamplifier circuit for differential input using ultra-low-noise/extra-high-input-impedance instrumentation operational amplifiers, a charge proportional to the impact load is output from both terminals, and the charge from the sensor is converted into a voltage. As the sensor also has favorable reactivity and the output voltage is as large as several tens of volts, the ratio of noise to the maximum measuring load is extremely low at 0.003%. The sensor thus offers an appropriate level of performance to enable measurement for the determination of load characteristics in the high-frequency domain.

2.4 Sensing stones

Piezoelectric-type triaxial acceleration sensors (Sensitivity 10 mV/G, Measurement Range 500G, Frequency range 2 to 10000 Hz within 5% deviation) were employed to measure ballast vibrational acceleration. These sensors leverage the semiconductor piezoelectric effect for detection of acceleration, and allow simultaneous measurement in three directions to cover all vibration occurring within a ballast structure. Shear strain is produced in a crystal lattice when mechanical external force is applied to a semiconductor crystal. Within the sensor body, each unit incorporates three separate sensing elements oriented at right angles to one another and includes semiconductor instrumentation pre-amplifier. Each axis is an individual independent channel in the data system.

Figure 4 shows a sensing stone consisting of a metal main body and a single piezoelectric triaxial acceleration sensor. The main body, measuring 10 cm in width/length and 2 cm in thickness, is made of

aluminum alloy with a specific density approximately equivalent to that of the ballast stones, and incorporates the sensor in its center. The acceleration sensor is sealed inside it to prevent local variations in measurement stemming from local contact conditions. The ratio of noise to maximum measurable acceleration is approximately 0.002 %. The acceleration sensor also offers an appropriate level of performance to enable measurement for the determination of load characteristics in the high-frequency domain.

2.5 Remote automatic measurement system

A remote automatic system was developed for extended-period measurement to allow safe, automatic determination of the dynamic response of existing track and enable remote observation without the need for personnel to enter the track area. A 168-channel high-speed (12 kHz) sampling PC-controlled data logger was employed for this purpose. Automatic measurement, data storage and calibration were achieved using the automatic measurement tool with a pre-trigger, and control/measurement were conducted by the RTRI via the Internet. Using this system, measurements were taken for a period of over one month.

3 DYNAMIC-LOAD MEASUREMENT TESTS

3.1 Measurement outline

A full-scale field experiment for measurement at a rail weld on a commercial service railway line was performed to evaluate the sensing sleeper's applicability. The pressure distribution induced by a running train on the bottom surface of the sleeper was measured. Figure 5 depicts the track-site installation, which was conducted on a straight section with a 60-kg per meter continuously welded rail (CWRs) track over PC3-type concrete mono-block sleepers laid on a 30 cm thick ballast bed over firmly tightened sandy soil ground on a conventional railway line in Kyushu, Japan.

Ballast renewal and trimming were first carried out in a 25 m straight section. The size and method of installation for the sensing sleeper were the same as those for existing sleepers. In the installation process, an existing sleeper was replaced with the sensing sleeper, which was fixed with regular fastening devices. This straightforward work was completed by simply tamping and trimming the ballast. Figure

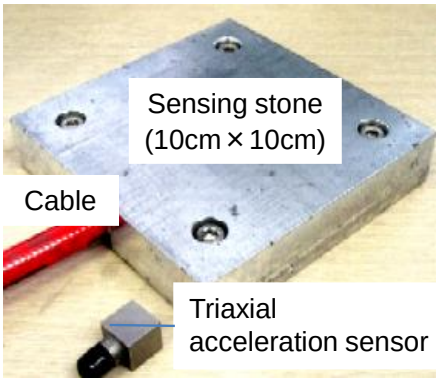

Figure 4: Triaxial sensing stone

Figure 5: Track-site installation

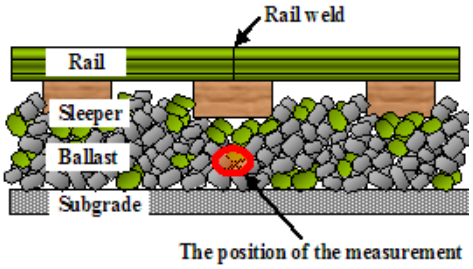

Figure 6: Measurement position for ballast-vibrating acceleration

6 shows the measurement position of ballast-vibration acceleration. The 3D motion sensor prototype was embedded in the ballast at a depth of 15 cm under the sleeper.

3.2 Load distribution from axle passage

Figure 7 shows sample results of measurement on the sleeper bottom to determine dynamic loading applied by the first axle on the lead coach bogie of a passenger express train traveling at 125 km/h through the measurement section. The figure shows the relationship between the wheel position and two-dimensional load distribution on the sleeper bottom. After the first axle arrives at the edge by the sleep-

er's front side, it moves gradually over the sleeper top before passing over the opposite edge of the sleeper. As the figure shows, a tendency exists by which the dynamic running load is not equally distributed throughout the sleeper undersurface – the values vary greatly by location, with large loads concentrated locally at specific points.

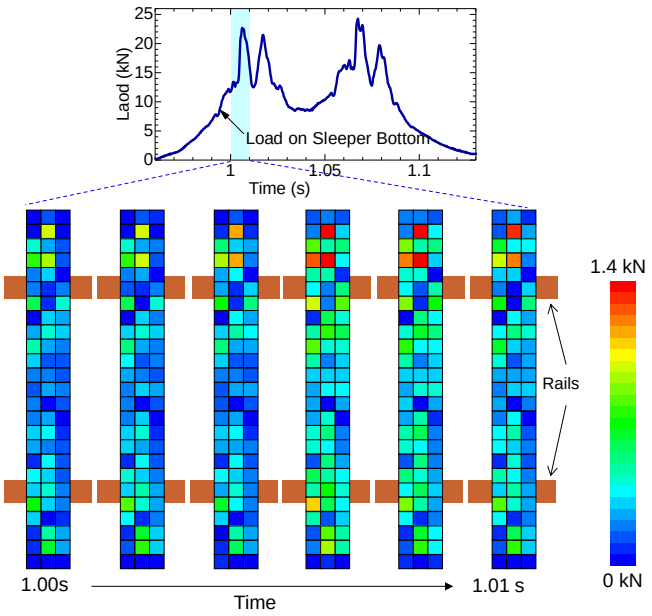

Figure 7: Example of measurement results for dynamic pressure on the sleeper

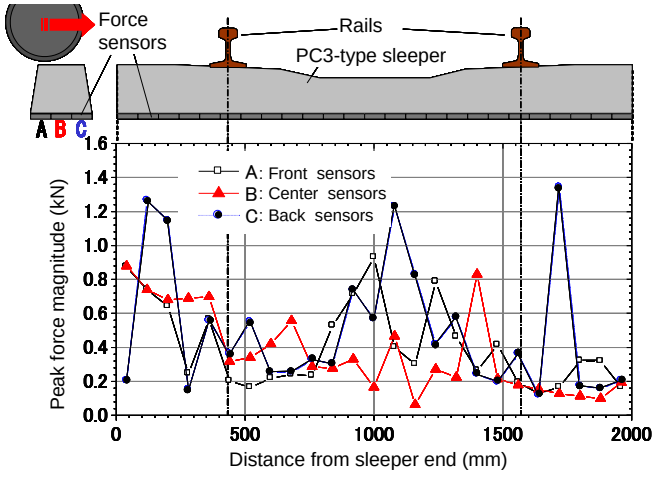

Figure 8: Measurement position for ballast-vibrating acceleration

3.3 Peak magnitude distribution

Figure 8 depicts peak-force-magnitude distribution in the time history of dynamic pressure on the sleeper bottom for all sensors in the short time during which the wheel moves over the sleeper top. The results show that the dynamic loads acting on the sleeper bottom are not supported uniformly over the whole of the sleeper underside. The loading varies greatly in relation to location, and is concentrated at specific contact points.

4 MEASUREMENT OF DYNAMIC RESPONSE IN TRAIN OPERATION

Impact loads from running trains are transferred to the ballast layer through rails, fastening devices and sleepers, and the dynamic loads of the ballast layer are considered to be directly influenced by the natural-frequency vibration characteristics of sleepers. Against such a background, the normal mode for a PC3-type sleeper was evaluated beforehand via experimental modal analysis in this research. Dynamic measurement of sleeper vibration, vibration loading on the ballast and ballast layer response was then conducted on an existing track during actual train passage. The results were then compared with those of the sleeper's normal modes.

4.1 Normal mode for a single sleeper

Figure 9 shows a sleeper excitation test involving experimental modal analysis. After measurement, vibrational force, response acceleration and individual modes can be identified by overlapping modes using experimental modal analysis. Such analysis

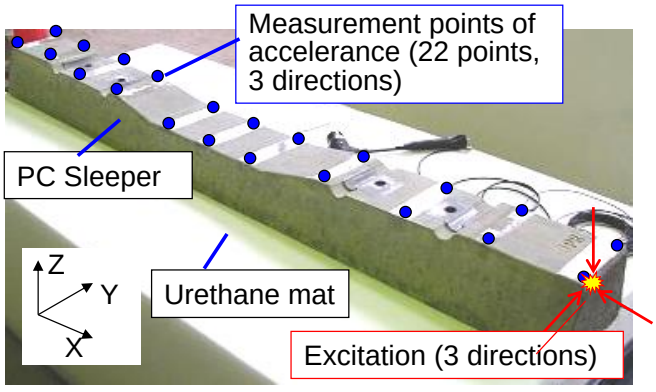

(a) Free-free condition

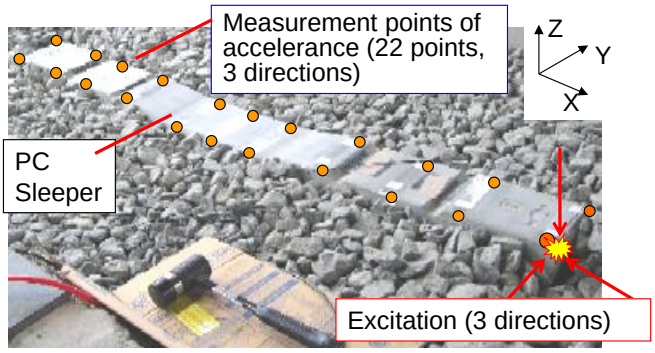

(b) In-situ condition

Figure 9: Full scale excitation experiment

was used to measure the set of normal modes for a PC3-type sleeper. The accelerance (acceleration/excitation power) at 22 points along the sleeper was measured. To reproduce approximate free boundary conditions, the sleeper was placed on a thick urethane mat. The modal analysis software (ME' scope VES, Vibrant Technology Co.) was used to analyze the measurement data obtained for 1 kHz or less; Table 1 and Figure 10 illustrate the natural modes and their mode shapes of the PC3-type mono-block sleeper identified by applying the experimental modal analysis. It is assumed that sleeper vibration on existing track corresponds to each of the mode shapes with the response peaking at a value close to the natural frequency.

However, in a similar experiment with the sleeper on a ballast layer, Remennikov et al. showed that natural frequency increases by up to about 40 Hz in comparison with that of a sleeper maintained in a free state. In addition to ballast layer support, the stiffness and mass of the rail and the rail fastening system were also added. Based on this, it is tentatively assumed that there is a slight difference between the identified natural frequencies and the peak frequencies measured in responses under real track conditions. Another tentative assumption is that under real track conditions and the given stiffness of the support, the natural frequencies of rigid translation modes the six degrees of freedom of the sleeper are actually lower than the first vertical bending natural frequency.

Table 1: Natural modes of the PC3-type sleeper

Mode shape	Natural frequency		Relative difference (B)-(A)/(A)
	Free-free condition (A)	In-situ condition (B)	
Rigid-body modes (Hz)			
(a) Rotation *y*	--	76	--
(b) Translation *y*	--	86	--
(c) Translation *x*	--	87	--
(d) Translation *z*	--	98	--
(e) Rotation *z*	--	112	--
(f) Rotation *x*	--	133	--
Bending modes (Hz)			
(g) 1st vertical	148	163	+10%
(h) 1st horizontal	241	243	+1%
(i) 2nd vertical	435	424	-3%
(j) 1st twisting	538	524	-3%
(k) 2nd horizontal	630	628	0%
(l) 3rd vertical	825	805	-2%

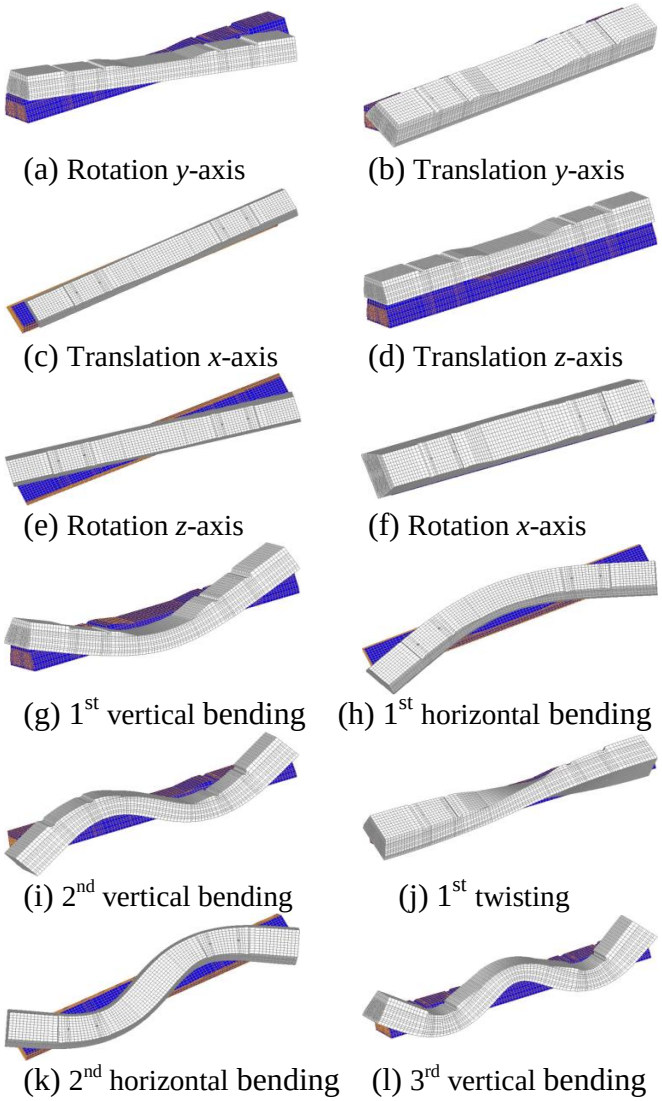

Figure 10: Mode shapes of a PC3-type sleeper

4.2 Installation of sensors

Field measurement was performed over a period of one month on a conventional railway section of the Tokaido Main Line in Japan. The field is a straight section with 60-kg/m-CWRs over PC3-type concrete mono-block sleepers laid on a 30 – 40 cm thick ballast bed over firmly tightened embankment ground.

The dynamic response was measured at 12 kHz sampling intervals for the vibration acceleration of the sleeper, the two-dimensional load distribution on the sleeper bottom, and the vibration acceleration of ballast pieces. Figure 11 (a) shows a side view of the measurement points, and Figure 11 (b) shows a top view of the sleeper. To measure the response of the sleeper up to the vertical third (w-shaped type) bending mode, sleeper vibration acceleration was measured at eight points on the sleeper top-surface. The dynamic loads acting on the sleeper bottom were measured using the sensing sleeper described previously. To compare average values of load distribu-

tion by location along the bottom plane of the sleeper, the sleeper was roughly divided into five sections. Figure 11 (c) shows the sections from SM1 to SM5, and each section housed 15 sensors. A total measurement value was then calculated for each section.

4.3 Load distribution on the bottom plane of the sleeper

Figure 12 shows sample load distributions on the sleeper bottom for each frequency and the corresponding sleeper deformation. These values were obtained by using a band-pass filtering after applying the fast Fourier transformation (FFT) to time history data measured over a period of 6.55 seconds (65536 time steps) as the train passed. The waveforms are smoothed by applying a Parzen window for a bandwidth of 20 Hz. As can be seen from the figure, both ends of the sleeper at 100 Hz underwent large vibration in phase while the center vibrated less, as with vibration under the first bending mode (Fig. 12 (a)). At 200 Hz, both ends of the sleeper vibrated strongly with a 90 degrees phase difference (Fig. 12 (b)). At 280 Hz, only the right side of the sleeper vibrated strongly (Fig. 12 (c)). At 340 Hz,

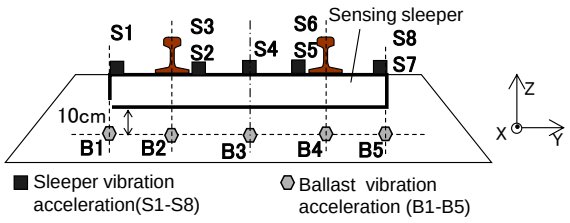

(a) Section side view

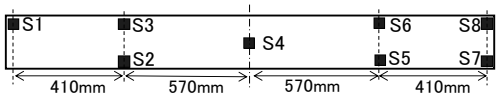

(b) Sleeper vibration acceleration (top view)

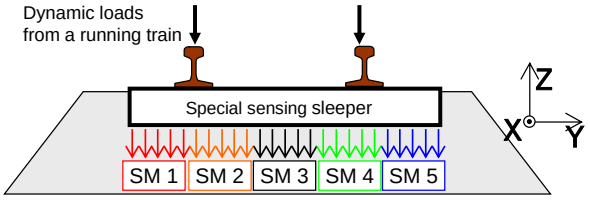

(c) Division into five sections on the sleeper bottom

Figure 11: Outline of field measurements

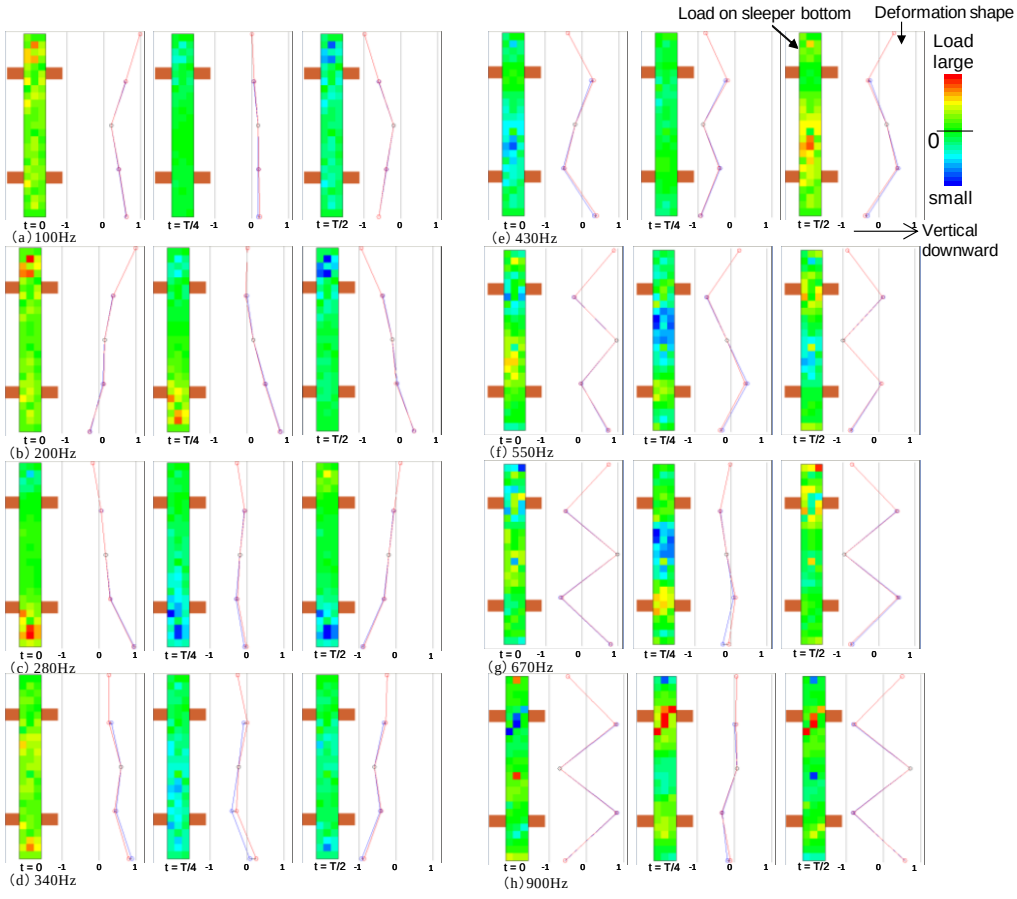

Figure 12: Load distribution on the sleeper bottom plane and corresponding sleeper deformation under conditions of train operation

the form of vibration became very complex, with the previously only slightly vibrating center part of the sleeper beginning to vibrate strongly together with both extremities (Fig. 12 (d)). At 430 Hz, close to where vibration was strong under the rail, the vertical second bending mode also appeared. At 550 Hz and 670 Hz, the vertical second and third bending modes appeared. Moreover, in this frequency range, which represents the sleeper's normal mode, the single torsion mode occurring here was not seen due to sleeper deformation. At 900 Hz, the third bending mode appeared in which the center and both ends of the sleeper vibrated strongly in phase (Fig. 12 (h)).

The six normal modes of a PC3-type sleeper were identified for frequencies of 1 kHz or less using experimental modal analysis in order to clarify the relationship between the sleeper's normal mode and the characteristics of load transmission to the ballast layer. The measurement results indicated that load distribution on the sleeper bottom becomes uneven in line with sleeper deformation. Even under existing track conditions with the passing of a train, vibration characteristics influenced by the sleeper's normal mode were clearly identified.

4.4 Impact force acting on the ballast layer

The characteristics of dynamic loads acting on the ballast layer were examined based on the measured dynamic response during train operation at a speed of 122 km/h. Figure 13 shows some exemplary time history response waveforms regarding the measured results. The linear amplitude spectra for loads exerted on the sleeper bottom, sleeper vibration acceleration and ballast vibration acceleration were calculated.

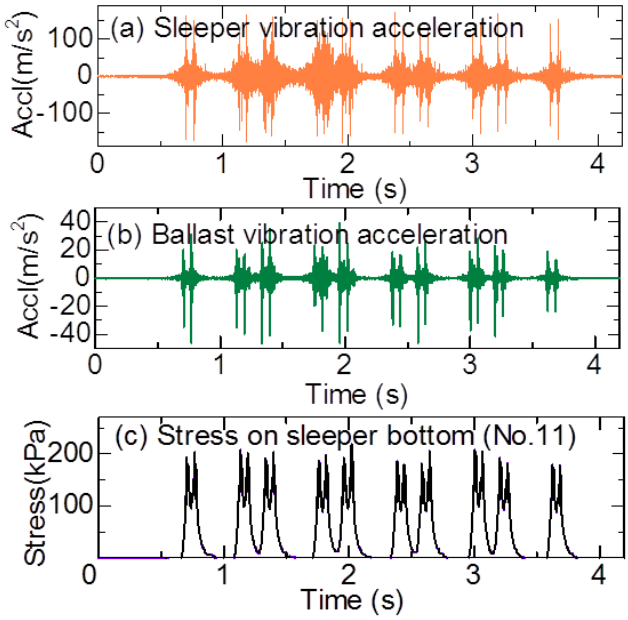

Figure 13: Exemplary measured results of response waveforms

Figure 14 presents linear amplitude spectra of the total resulting force regarding the rail seat force and the response loads exerted on the sleeper bottom. These values were obtained by applying FFT to data obtained over a period of 6.55 s (65 536 points) as the train passed, and were smoothed by applying a Parzen window for a bandwidth of 20 Hz. The figure shows that impact loads acting on the ballast layer have extremely wide-band frequency components.

Comparison of linear amplitude spectrum configurations for rail seat force and loads on the sleeper bottom reveals that both have very similar frequency characteristics. It can therefore be inferred that for impact loads acting on the sleeper through the rail seat from the bottom surface of the rails, transfer to the ballast layer through the sleeper bottom remained almost unchanged.

Most frequency values associated with peak responses among amplitude spectrum configurations are seen near frequencies approximately corresponding to the natural modes of a sleeper. For example, the measurement results show several resonance frequency peaks around 100, 200, 400 and 800 Hz that largely coincide with the bounce mode (translation mode) and the first, second and third vertical bending modes of the PC sleeper, respectively. In the low-frequency domain in particular, the amplitudes of loads acting on the sleeper bottom are larger than those of the rail seat force. These results clearly indicate that loads acting on the ballast layer are influenced by the vibration characteristics of sleeper natural frequency.

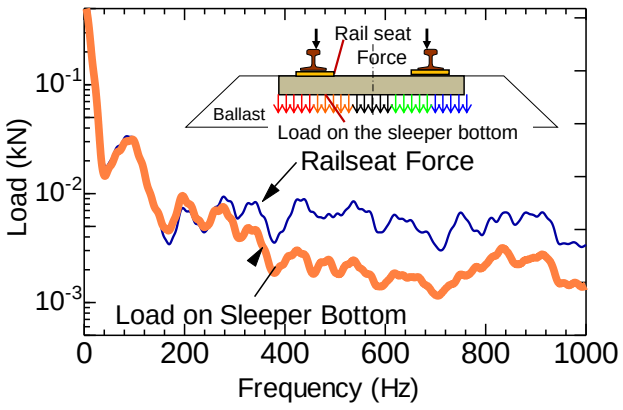

Figure 14: Linear amplitude spectra of rail seat force and loads on the sleeper bottom

4.5 Sleeper and ballast acceleration responses

Figure 15 shows the linear amplitude spectra of the sleeper and of the ballast vibration acceleration at a point 10 cm beneath the sleeper bottom. The derived figure indicates that the impact loads acting on ballast show large response amplitudes not only around the low-frequency area but also in the high-frequency domain exceeding 100 Hz. This means that the impact load acting on ballast consists of broadband components with vibrations from low to high frequency. Among these, the load components of the high-frequency domain result from the sharp impact load peaks generated momentarily by the wheel-rail contact mechanism.

As the rocks from which ballast is made are usually categorized as soil materials, and also because the dominant frequency during axle passage was measured in the low-frequency domain of several to around 30 Hz, earlier studies relating to conventional ballast tracks generally involved little attention to this frequency range. However, the results of field measurements clarified that impact loads acting on the ballast layer contain broadband load components from low- to high-frequency domains, and that very high-frequency components definitely act on the ballast layer. To reduce ballast degradation stemming from traffic impact loads on ballasted track, it is thus insufficient to focus solely on the low-frequency behavior of ballast pieces. It is essential to reduce the strong impact-load components of these high-frequency bands.

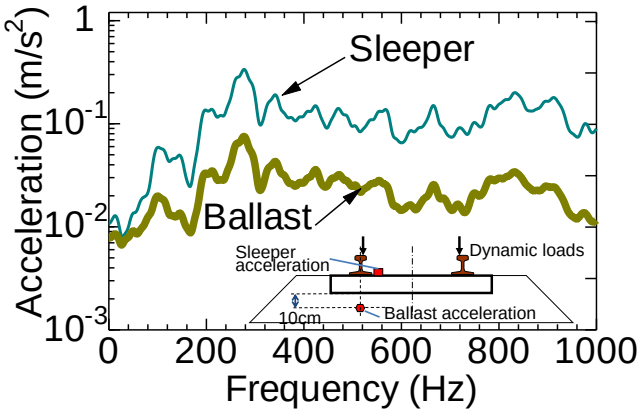

Figure 15: Linear amplitude spectra of response acceleration

4.6 Sleeper and ballast displacement response

Figure 16 shows linear amplitude spectra of response displacements with respect to the sleeper and the ballast pieces. Several response acceleration peaks appear in line with the natural mode of the sleeper and the response acceleration itself. The ballast displacement amplitude in the figure decreases rapidly in inverse proportion to the second power of frequency as the frequency increases. When the frequency is 100 Hz, the magnitude of the ballast amplitude is small at several ten to the power of minus 7 meters. At about 800 Hz (corresponding to the third bending mode of the sleeper), the value is extremely small at several 10^{-9} m.

Regular discrete element (DE) analysis reveals the phenomenon of force transformation between ballast pieces due to changes in the center of gravity of each piece in a rigid body and the occurrence of sedimentary intrusion among pieces. The results of such investigation highlight the movement of ballast pieces due to the rigid-body motion and frictional sliding motion that occur among them. Regular DE analysis requires that a significant degree of rigid-body displacement should occur in each ballast piece. However, as may be apparent from the measurement results, ballast displacement generated by the high-frequency components of impact force in the ballast layer is less than that observed in DE analysis in several figures, and that generated by high-frequency components of impact force added to the ballast layer is much less.

Considering the results of ballast behavior monitoring on existing ballasted track, the rigid-body motion and frictional sliding motion of ballast pieces alone do not fully explain the phenomenon of impact load transfer in the inner part of ballast, especially in regard to the high-frequency behavior of ballast pieces. Accordingly, to clarify propagation phenomena related to impact loads in a ballast layer, it is necessary to evaluate the characteristics of elastic-deformation behavior relating to angularities near contact points between ballast pieces, and to clarify the elastic wave propagation characteristics observed inside each ballast piece.

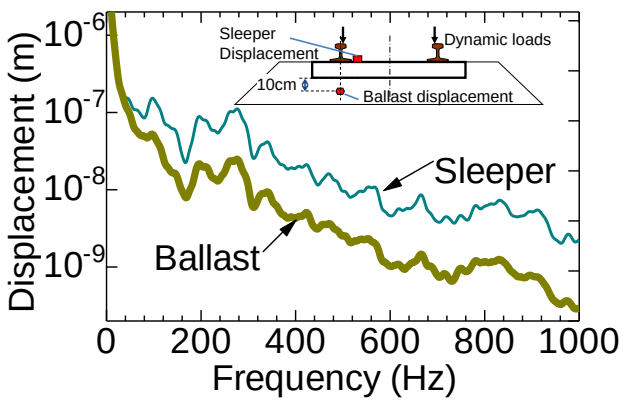

Figure 16: Linear amplitude spectra of response displacement

4.7 Ballast-related reduction of impact loads

Figure 17 shows the frequency response function (FRF) observed between masses of sleeper ballast as determined from linear amplitude spectra of sleeper displacement and ballast displacement. It indicates the magnitude of displacement (or acceleration) occurring in ballast pieces at a depth of 10 cm under the sleeper when sine wave displacement (or acceleration) with an amplitude of 1 is applied to it. In the figure, the amount below 1 represents the magnitude of the reduction effect of loading energy in ballast with a thickness of 10 cm. The displacement and amplification ratios are shown in Figure 16, which indicates that impact-load components decrease in magnitude to about one third to one fifth in the high-frequency domain of about 100 to 200 Hz or more, irrespective of frequency. Although the ballast is only 10 cm thick in this case, the results indicate that the ballast layer has an extremely positive load reduction effect for high-frequency components of impact loads.

However, the low-frequency domain also exhibits an amplification ratio near 1. It is readily apparent that the ballast layer has almost no effectiveness in reducing impact-load components in the low-frequency region of less than 100 Hz. The figure also indicates that the mechanisms of ballast behavior differ completely in the high-frequency domain of 100 to 200 Hz or more and in the lower-frequency domain. By increasing the ballast layer thickness, the high-frequency components of impact loads acting on it can be eliminated completely but the related low-frequency components must also be eliminated completely in the stage before impact loading reaches the ballast layer surface. One way of achieving this is to insert soft shock-absorbing materials beneath the sleeper.

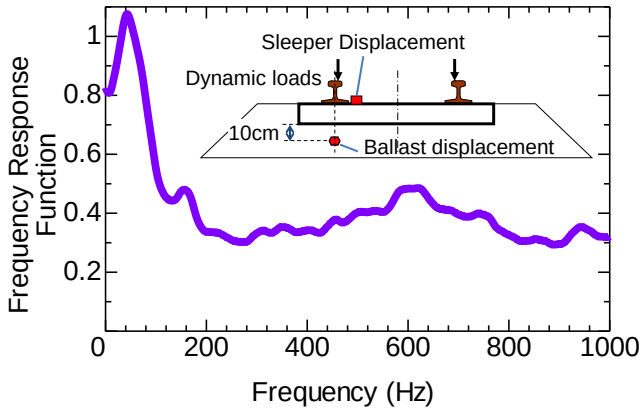

Figure 17: Sleeper-ballast frequency response function (FRF)

5 RELATIONSHIPS BETWEEN STRESS AND STRAIN IN BALLAST BEHAVIOR

5.1 Stress-strain curve of a ballast layer

Figure 18 shows the average curve of the equivalent stress-strain relationship (per 30 cm of ballast layer in terms of thickness) calculated at five sections under the sleeper as illustrated in Figure 11 (c). The figure shows the relationship between the amplitudes of linear spectra for response strain and the amplitudes of linear spectra for response stress with all frequency components.

Each frequency in the figure indicates the value in the response spectrum. In addition, frequency components higher than those of values given in the figure are concentrated linearly near the origin, forming a sharp slope at the beginning of the curve. The curve's slope represents the elastic modulus of the ballast layer, that is, its hardness. Regarding ballast behavior, clear linearity in the strain-stress relationship is observed near the origin where strain is small (that is, in the high-frequency domain over several tens of Hz). The whole ballast layer synchronizes integrally as a single continuous elastic body and exhibits sufficient reaction to impact loads. However, when strain becomes large (that is, in the low-frequency region of 10 Hz or less), the ballast layer deforms easily and significantly. That is, the layer can be considered to act as an elastic body subject to high-frequency components and demonstrates a strong load reduction effect. However, with low-frequency components, the ballast itself deforms significantly and the layer cannot provide a sufficient level of resistance.

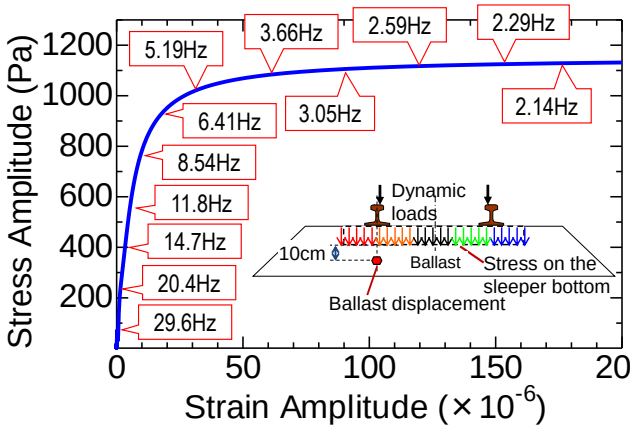

Figure 18: Stress-strain relationship of the ballast layer

5.2 Frequency dependency of the ballast layer dynamic elastic modulus

Figure 19 shows the dynamic elastic modulus per 30 cm of ballast layer thickness. The figure shows that the ballast layer's dynamic hardness varies drastically with frequency, and that its dynamic elastic modulus tends to increase gradually with impact load frequency. The layer has a dynamic elastic modulus of about from 200 MPa to 2 GPa in relation to the load components in the frequency band of 100 Hz or more. Rocks used for ballast usually provide a static elastic modulus of about from 40 GPa to 60 GPa when intact. As the figure shows, although the dynamic elastic modulus of the ballast layer is 10 to 100 times less than that of intact rocks, it is still strong enough to act as soil material for a ballast layer.

Regarding the load component of the frequency band lower than 100 Hz, the figure shows that the dynamic elastic modulus rapidly decreases with frequency. This corresponds to extreme softening of the ballast layer, meaning that it provides unsufficient resistance to the low-frequency components of impact loads.

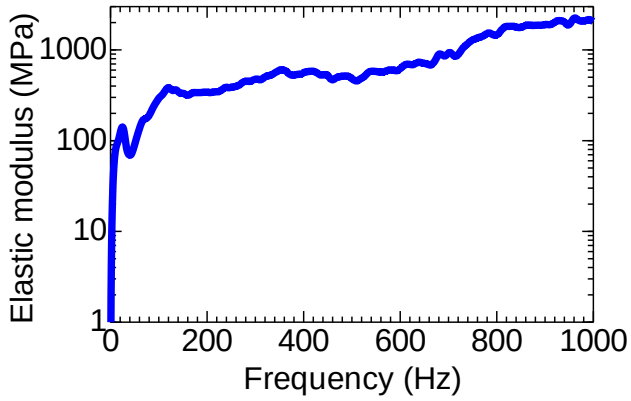

Figure 19: Equivalent elastic modulus of the ballast layer

5.3 Mechanism behind ballast layer frequency dependency

The previous chapter discussed the resistance of the ballast layer based on its elastic modulus and other related measurement data. The results showed that the high-frequency components of impact loads can be explained in consideration of the layer's spring modulus. However, for low-frequency components, the elastic modulus alone does not explain the situation. Accordingly, this chapter further examines the evaluation axis in relation to mass with particular focus on low-frequency components.

The equation of motion for a ballast layer is given as:

$$ma + cv + ku = f \ , \quad (1)$$

where *a*, *v*, *u* and *f* respectively denote acceleration a $a = \partial^2 u / \partial t^2$, velocity $v = \partial u / \partial t$, displacement and external force. The coefficients *m*, *c* and *k* respectively represent mass, the viscosity coefficient and the stiffness coefficient. The first term *ma* on the left-hand side of Equation (1) is the inertial term, the second term *cv* is the viscous term, and the third term *ku* is the stiffness term. On the right-hand side, *f* is the load term. Structural damping is assumed here rather than the viscous term (the second on the left-hand-side), which means the damping effects are considered based on the values of the imaginary part of the complex number of the stiffness term. Accordingly, the equation of motion is as follows:

$$ma + ku = f \quad (2).$$

The magnitude of contribution of the inertial term and the stiffness term in this equation can be compared by evaluating the equivalent mass proportional to acceleration and the equivalent stiffness modulus proportional to displacement based on measurement data for the ballast layer.

Figure 20 shows the apparent mass and the dynamic stiffness of the ballast layer as calculated from the spectral characteristics of measurement data. As the units differ, the calculated results are normalized (that is, divided by each maximum) so that the maximum is 1. An apparent mass close to 1 in the figure signifies that ballast behavior is dominated solely by the effects of the inertial term. When the

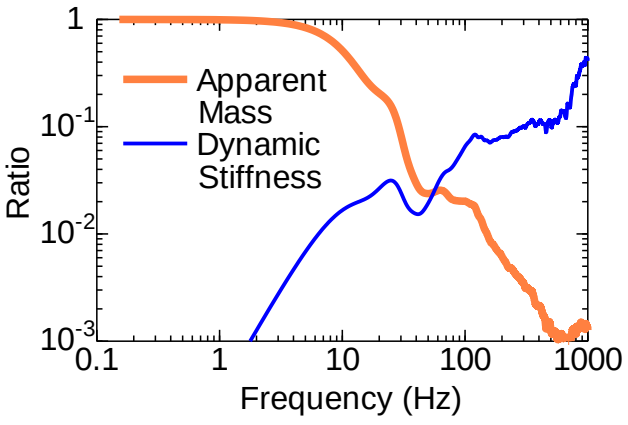

Figure 20: Apparent mass and dynamic stiffness of the ballast layer

dynamic stiffness value is close to 1, behavior is dominated only by the effects of the stiffness term. The figure shows that the apparent mass has a constant value of around 1 in the frequency region of about 10 Hz or less. For impact-load components with a frequency of 10 Hz or less, ballast behavior depends mostly on the inertial term. Accordingly, the ballast layer has greater resistance with increased mass.

As discussed in the preceding sections, the figure shows that the dynamic stiffness only slightly contributes to ballast behavior in the low-frequency region of 10 Hz or less. In the high-frequency domain exceeding 100 Hz, behavior is determined solely by the characteristics of ballast stiffness.

Additionally, for frequencies of 10 – 100 Hz, it can be inferred that the effects of ballast stiffness and mass depend on synergy or rivalry, and that the ballast layer will exhibit complex behavior.

6 MODELING OF BALLAST PIECES AND FINITE ELEMENT NORMAL-MODE ANALYSIS

This chapter describes finite element vibration analysis of ballast aggregate to clarify frequency characteristics up to the high-frequency domain. In the investigation, ballast stones were used to express a polyhedron model based on the three-dimensional discrete element (DE) method. A finite element (FE) model was built in reference to the numerical arrangement of ballast stones and related contact data. Train loads can be applied to this model to simulate associated behavior and clarify the stress distribution of ballast aggregate with respect to impulse loading based on vibration analysis conducted using the model.

6.1 FE modeling for individual ballast pieces

Measurement was first performed to determine the vertex coordinates of around 4000 ballast pieces using a contact-type three-dimensional digitizer. Figure 21 shows the measurement instruments used. When the equipment's switch pedal is pressed, the three-dimensional coordinates at the tip of the digitizer probe are measured automatically and sent to the PC as text data. Based on the measured coordinates with mutual connection of the vertices in straight lines, the configuration of each crushed stone can be represented numerically as a three-dimensional polyhedron consisting of an assemblage of triangular planes. The automatic generation algorithm applied was newly developed to allow objective and efficient determination of polyhedron shapes from the vertex coordinates measured. The algorithm is based on two concepts: (1) a polyhedron consists of a set of triangles, and (2) it becomes convexly configured to the greatest degree possible.

Figure 22 shows sample images of existing ballast and digitized models based on numerical data from measurements. Using the algorithm, the measured vertex coordinates are expressed numerically as DE polyhedron models. The individual models are then converted into aggregates of solid tetrahedral FE meshes (3D second-order FE elements) with intermediate nodes between edge pairs. A sufficiently fine mesh size of 10 millimeters was adopted to support the production of reliable stress information, the accurate representation of stress distribution, the determination of local stress concentration and the precise representation of normal mode frequencies. The figure shows that the DE polyhedron and FE aggregate models generated closely reproduce the actual angular geometry of ballast stones.

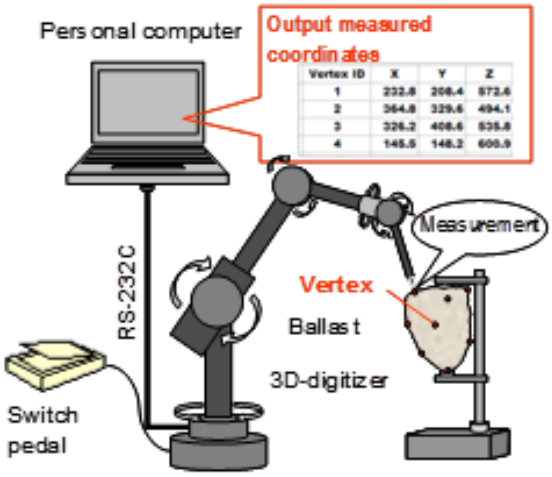

Figure 21: Digitization of ballast piece shape

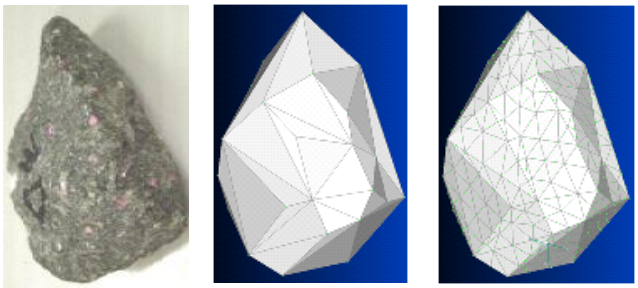

(a) Ballast (b) DEM Model Model (c) FEM

Figure 22: Sample pictures of existing ballast and digitized models

Table 2. Physical properties of ballast

Item	Ballast
Density ρ	2,700 kg/m^3
Young's modulus E	30 GPa
Poisson's ratio ν	0.2
Structural damping parameters η	0.01

Table 2 shows the ballast physical properties used in this study, including density, Young's modulus and Poisson's ratio. The ballast density adopted was the laboratory experimental value obtained from specific gravity tests, while Young's modulus and Poisson's ratio were derived from previously published reports. General concrete structure values were adopted for the structural damping coefficient.

6.2 Normal-mode analysis for individual ballast pieces

After the individual DE polyhedron models had been converted to aggregates of the FE tetrahedral models, 60 cases of FE normal-mode analysis were performed, yielding a set of normal modes for individual ballast pieces. Figure 23 shows a sample result of normal-mode analysis related to the first-, second- and third-order normal modes of a ballast piece. The contours in each figure show von Mises strain values, and the first, second and third normal modes are the respective modes accompanied by elastic deformation such as bending and torsion for ballast pieces.

Figure 24 shows the relationship between the first- and second-order natural frequencies for 60 ballast pieces. All natural frequencies of the pieces were identified in the very high-frequency domain of more than 11 kHz. In addition, Figure 25 shows the average values and standard deviations of natural frequencies related to normal modes from the first to the fourth order.

6.3 FE modeling of ballast aggregate

Figure 26 shows the procedure for the creation of a ballast aggregate FE model. First, 89 pieces from the individual ballast model (the polyhedral rigid-body DE type) were placed randomly and homogeneously in the air above rectangular box frames on the roadbed. The blocks were then allowed to fall freely and compressed with a loading plate from the ballast upper surface using the 3DEC discrete element method, and time-dependent 10 kN homogeneous loading

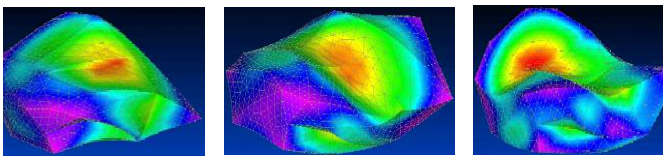

(a) First order (15.0 kHz) (b) Second order (13.3 kHz) (c) Third order (20.2 kHz)

Figure 23: Sample results of normal-mode analysis

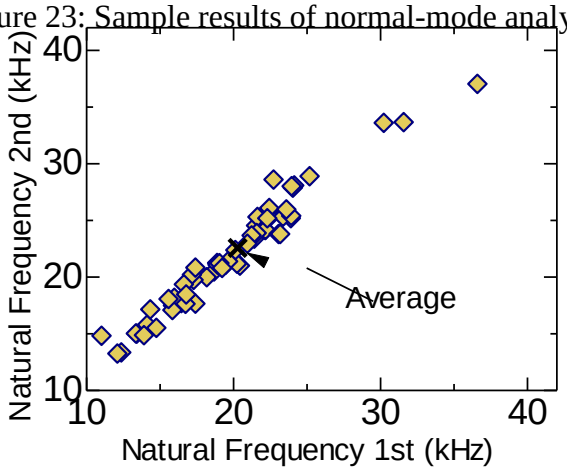

Figure 24: Distribution of natural frequencies

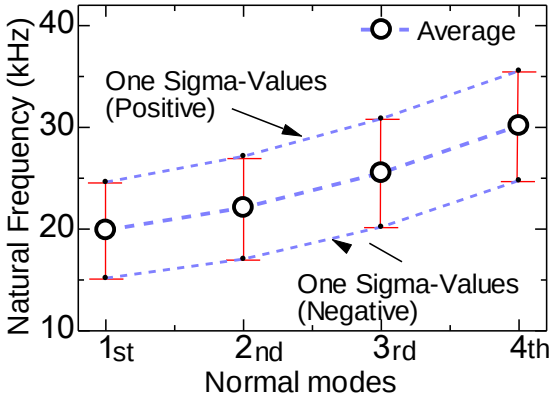

Figure 25: Average values of natural frequencies

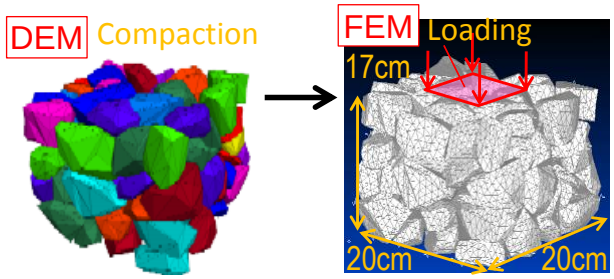

Figure 26: Procedure for creation of an FE model of ballast aggregate

was added to the loading plates. After 0.5 s of compaction, the plates were separated from the ballast and the blocks were left unloaded for 1 second. In this case, the normal stiffness between ballast pieces

was set to an extremely large value (2,000 GPa/m) to reduce the amount of penetration between pieces. The friction angle between ballast pieces was also set to a small value (5 degrees) for effective compacting of pieces.

Next, all individual ballast pieces (polyhedron DE rigid models) were converted into clumps consisting of small FE elements (the tetrahedron second-order elastic type) split into 10 mm meshes with geometry and contact-point information maintained. Each polyhedron DE rigid model was divided into 4000 to 5000 tetrahedron elastic FE elements. The finished FE analysis model was 20 cm in width and length and 17 cm in height, and had more than 460,000 tetrahedron FE elements.

The contact-point information between ballast pieces was modeled as a set of extremely hard 3 dimensional springs (spring stiffness k equals 300 GN/m) with no length, which connected the nodes of elements in three axial directions related to the contact pair of blocks at each contact point. The stiffness of the contact springs was set much higher than those of the tetrahedron FE elements so that the shape of the springs would remain almost unchanged against external forces. Frictional effects were ignored in this analysis, and only mutually connected contact pairs were used. Accordingly, the spring functions on the contact points were represented by the local deformation of ballast angularities composed of assemblages of several tetrahedron finite elements adjacent to contact points.

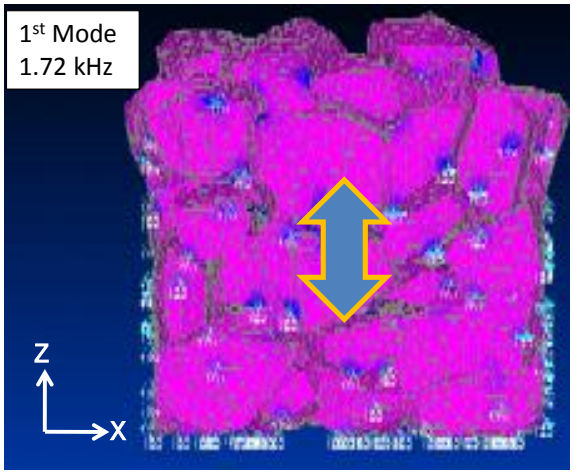

Figure 27: First-order natural frequency mode (side view)

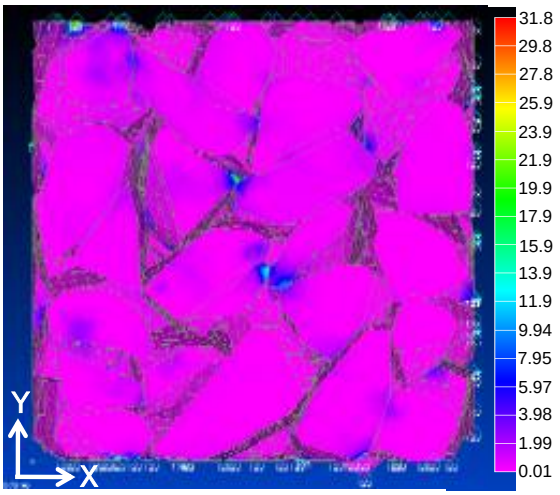

Figure 28: Stress distribution of the first-order natural frequency mode: top view of x-y cross-section (z = 0.132 m)

6.4 FE normal-mode analysis of ballast aggregate

By applying finite element normal-mode analysis to the ballast aggregate FE model, a set of normal modes related to the aggregate was obtained. Figure 27 shows the first-order natural frequency mode of the ballast aggregate as determined from the numerical results of normal-mode analysis. As the figure shows, the first-order natural frequency mode of the aggregate is such that its whole mass underwent repeats vertical elastic expansion and shrinkage within the restrictions of the square frame.

The normal frequency of the first-order normal mode, which represents the vertical motion of the entire aggregate, is 1715 Hz. This is much lower than the normal frequency of individual ballast pieces. The respective normal frequencies of the second- and third-order normal modes are 1980 Hertz and 2030 Hertz. The structure of actual ballast is larger than that of this model. Accordingly, the results suggested that actual ballast will have a similar normal mode in the lower frequency domain to that of the analytical results.

Figure 28 shows the distribution of strain with respect to the horizontal cross-sectional plane with a height of 13.2 cm, and indicates that only a few angularities (sharp edges) are adjacent to contact points. Among all angularities of the ballast aggregate, only these ones would deform locally and act as elastic springs, with most other parts of the aggregate vibrating as a rigid body. The results show that the dynamic loads acting on ballast aggregate are not supported uniformly all over its individual pieces. They vary greatly in relation to location, and exhibit concentration around certain contact points among all angularities. These results indicate that most portions in ballast aggregate subjected to dynamic loading vibrate homogeneously and elastically. Never-

theless, only a few specific angularities adjacent to stress concentration areas vibrate violently.

6.5 Responses of ballast aggregate to actual traffic loading

The time-history response waveforms of internal stress in ballast pieces were calculated numerically by inputting measured loading waveforms to the bottom surface of a sleeper when a passenger express train moved over the top surface of the previously described ballast aggregate model.

Figure 29 shows actual waveforms of vertical loading (as measured in an 8 cm in width and length cross-sectional area on the bottom surface of the sleeper) applied by the first and second axles of a lead coach bogie when a passenger express train moved through the test section at about 122 km/h, and indicates that the axles passed immediately above the sleeper center at around 0.06 and 0.12 s, respectively. In the FE analysis, the measured time history waveforms were uniformly input to the four points around the center area of the top surface of the ballast aggregate model. The calculation time interval was set to Δt = 10 μs.

Figure 30 shows the von Mises stress distribution

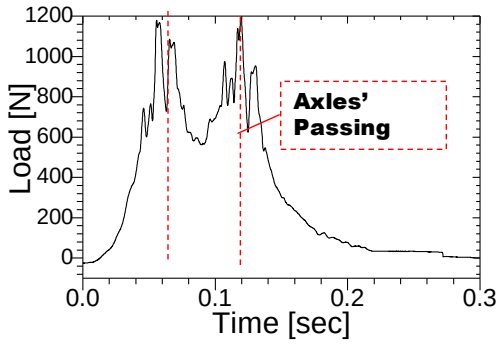

Figure 29: Measured waveform of loading on the sleeper bottom surface

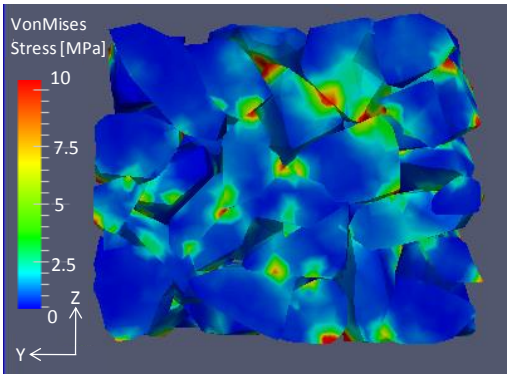

Figure 30: Internal distribution of ballast aggregate stress

in the ballast aggregate at t equals 0.055 second when the load peaks appeared as the first axle of the lead coach bogie passed immediately above the sleeper center. It can be seen that the dynamic stress induced by a passing train on ballast was not distributed uniformly throughout the aggregate. Significant stress was concentrated locally around specific contact points. The analytical results show that the 43 MPa maximum stress within the time history occurred with external loading of 1.2 kN (0.19 MPa).

Although the magnitude of the analytical model was extremely small, the ratio of internal maximum stress to external loading reached approximately 230 as a minimum. The unconfined compressive strength of ballast pieces was 60 – 100 MPa and the maximum stress in this analysis showed a lower value. However, it can be reasonably estimated that angularity failure will occur around stress concentration points when excessive dynamic external forces act on the ballast surface.

7 ANALYSIS OF WAVE PROPAGATION WITHIN BALLAST AGGREGATE

7.1 Analytical conditions

Dynamic loading acting on the body surface propagates in ballast aggregate as impact waves. This chapter describes transient response analysis performed to evaluate the characteristics of wave propagation in ballast aggregate in response to impact

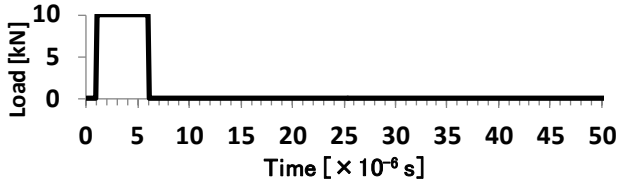

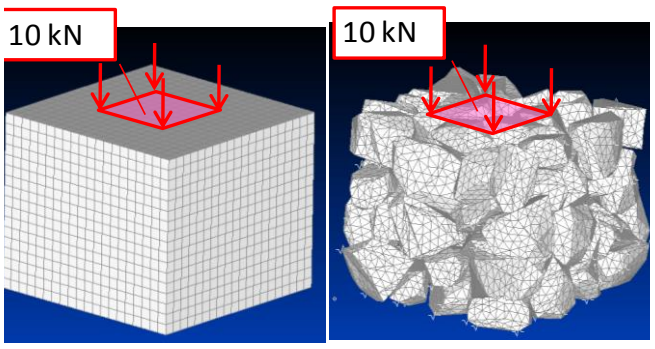

(a) Intact Rock (b) Ballast Aggregate

Figure 31: Models and impact loading

loading.

Figure 31 shows the vertical impact loading waveforms applied and the two types of numerical models used. One is an intact-rock model consisting of 6800 cubic FE elements with an edge length of 1 cm each with a continuous homogeneous elastic body. The model dimensions were 20 × 20 × 17 cm in height. The other is the previously described ballast aggregate FE model. Time-dependent loading waveforms were applied vertically to an 8 × 8 cm area around the center of the top surface of each model via a single rectangular pulse. With the amplitude and pulse length respectively set to 10 kN and 5 μs, the stress distribution characteristics of the ballast aggregate at every time step of Δt = 1.0 μs were calculated.

7.2 Stress distribution

Figure 32 shows the distribution of von Mises stress on the vertical section passing through the central axis at each time step. For the intact rock shown in Figure 32 (a), the impulse wave gradually spreads downward with uniform velocity, reaching the bottom surface at 47μs. In contrast, for the ballast aggregate shown in Figure 32 (b), the impulse wave generally follows a complex course with four steps: (1) The wave and impact force propagates through the inner part of the rock after it is hit with an impulse hammer at the same speed as that in the case of the intact rock. (2) Most waves remains in the inner part of the rock and undergoes repeated diffusion and reflection. (3) Some waves are transmitted through contact points to other rocks. (4) Waves reaching adjacent rocks diffuses in their inner parts, and some propagates to the next rock through other contact points. At 60 μs in Figure 32 (b), the wave's leading edge reaches the middle part of the model, but a large number of strong waves exhibit repeated diffusion and reflection in the inner parts of the upper rocks.

7.3 Time history response of contact stress

Figure 33 shows the time history response waveforms of von Mises stress for three arbitrary contact points located at different depths near the central line under the loading points. As the distance of measuring points from the loading point increases, the number of high-frequency vibrating components decreases, waves become smoother and the times at

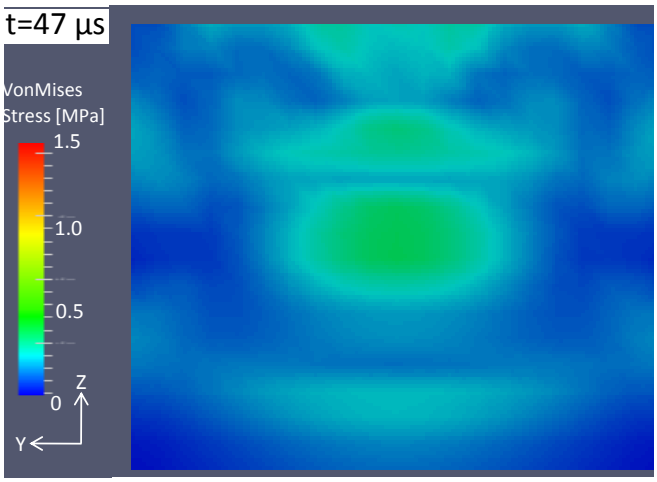

(a) Intact Rock

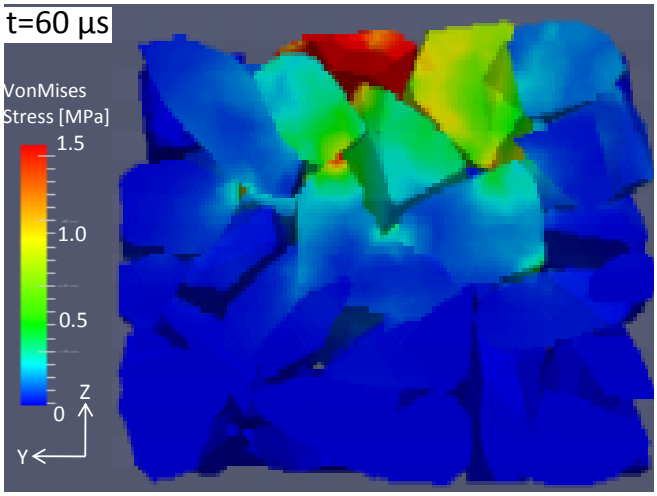

(b) Ballast Aggregate

Figure 32: Distribution of von Mises stress in a vertical section

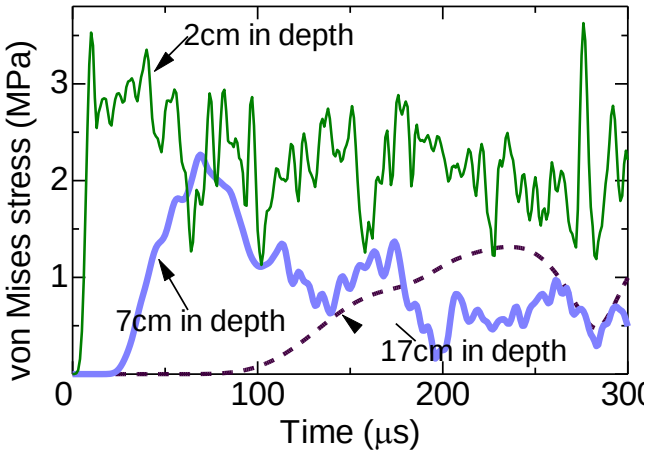

Figure 33: Time history response waveforms of von Mises stress

which peak responses occur in each stress waveform time history become later.

Based on the peak value occurrence time in the stress waveform time history, elastic wave velocities were calculated for both models. This velocity in intact rock reaches 3610 m/s, whereas that in ballast aggregate model is only 710 m/s The results of this analysis showed that elastic wave velocity in ballast is one-fifth of that seen in intact rock. Elastic wave velocity in a hard rock mass is generally 3000 to 5000 m/s, while that in real ballast aggregate is approximately 400 m/s. This analysis numerically reproduced the mechanisms by which wave propagation velocity is reduced and wave motion decreases greatly inside a ballast layer. It should be noted that the study involved only elastic body analysis, which does not incorporate material nonlinearity.

8 CONCLUSIONS

This paper details the principle, design and fabrication of a special sensing sleeper and describes field experiments performed to confirm its applicability. Field measurements were taken for more than a month to clarify the transmission characteristics and reduction mechanism of impact loads within a ballast layer. The results of frequency domain analysis for the values measured allowed quantitative evaluation of the impact load reduction effect in the ballast layer and the dependency of strength characteristics on frequency with respect to the initial stage of ballast degradation. The paper also describes finite element vibration analysis of ballast aggregate to clarify frequency characteristics up to the high-frequency domain. The modeling method involved the use of ballast stones in the form of a polyhedron model with the three-dimensional DE approach. A FE model was built based on the numerical arrangement of ballast stones and related contact data. The results obtained from the study are outlined below.

A sensing sleeper with numerous ultra-thin impact force sensors attached to its underside was developed to measure dynamic pressure distribution on the sleeper bottom, and its sensory performance was confirmed. The dynamic running load induced by passing trains was not distributed uniformly throughout the sleeper undersurface. Rather, it varied significantly with location, and tended to be concentrated at specific contact points. The impact loads acting on a ballast layer were found to consist of extremely wide-band frequency components of low- to high-frequency vibrations. It was confirmed that load components of the high-frequency domain act on the ballast layer. Ballast layer loading is influenced by the vibration characteristics of a sleeper's natural frequency. Uneven load distribution on the sleeper bottom was observed in line with sleeper deformation. Even under existing track conditions with train passage, vibration characteristics influenced by the sleeper's normal mode were clearly identified.

In a ballast layer, although impact loads decreased substantially to a load component of 100 Hertz or more, lower-frequency components decreased only slightly. For a frequency of 100 Hz, the amplitude of ballast displacement is small at several tens to the negative seventh power meters. At about 800 Hz, the value is extremely small at several tens to the negative ninth power meters. To clarify propagation phenomena related to impact loads in a ballast layer, it is necessary to evaluate the characteristics of elastic-deformation behavior relating to angularities near contact points between ballast pieces, and to determine the characteristics of elastic wave propagation inside each ballast piece. The results of frequency domain analysis allowed quantitative evaluation of ballast layer impact load reduction. The ballast layer was found to have two characteristics depending on dynamic stiffness. For load components over 100 Hz, the ballast layer has high rigidity, resists dynamic loads sufficiently and can reduce impact loads adequately. However, with the low-frequency range, the layer easily deforms and cannot reduce load components. Therefore, by increasing the ballast layer thickness, the high-frequency components of the impact loads acting on it can be eliminated completely, but the related low-frequency components must also be eliminated completely in the stage before impact loading reaches the ballast layer surface. One way of achieving this is to insert soft shock-absorbing materials beneath the sleeper.

Based on FE normal-mode analysis regarding individual ballast pieces, all normal modes for such pieces were identified in the very-high-frequency domain of more than 11 kHz. However, the ballast aggregate structure indicated that the normal frequency of the first-order normal mode is much lower than that of individual ballast pieces. Input of measured train loads to the ballast aggregate model clarified that dynamic stress was not distributed uniformly throughout ballast aggregate. Large amounts of stress were concentrated locally around specific contact points. The mechanisms by which wave propagation velocity inside a ballast layer is reduced and wave motion inside it is greatly reduced were numerically simulated using only elastic body analysis without consideration of material nonlinearity.

9 REFERENCES

Aikawa, A., Urakawa, F., Abe, K. and Namura, A., "Dynamic Characteristics of Railway Concrete Sleepers using Impact Excitation Techniques and Model Analysis," *WCRR2011*, 2011.

Aikawa, A., "DEM modeling techniques for dynamic analysis of ballasted railway track", *2nd International FLAC/DEM Symposium*, 2011.

Aursudkij, B., "A laboratory study of railway ballast behaviour under traffic loading and tamping maintenance," *Ph.D. Thesis, University of Nottingham*, 2007, 215p.

Azéma, E., Radjai, F. and Saussine, G., "Quasistatic rheology, force transmission and fabric properties of a packing of irregular polyhedral particles," *Mechanics of Materials*, 41(6), 2009, pp. 729-741.

Azéma, E. and Radjai, F., "Stress-strain behavior and geometrical properties of packings of elongated particles," *Physical Review*, E, 81(5), 2010.

Fujimoto, T. and Arif, S. T., "Sheet type impact force sensor by the use of Piezoelectric film (mechanical system)," *Transactions of the Japan Society of Mechanical Engineers*, JSME, C, Vol.73, No. 725, pp.184-191 (in Japanese).

Indraratna, B., Lackenby, J. and Christie, D., "Effect of confining pressure on the degradation of ballast under cyclic loading," *Géotechnique*, 55(4), 2005, pp. 325-328.

Ishida, M., Namura, A. and Suzuki, T., "Track settlement measurements and dynamic prediction model based on settlement laws," *WCRR2003*, 2003, pp. 728-737.

Itasca Consulting Group, Inc.,"3DEC – 3 Dimensional Distinct Element Code", Ver. 4.10 User's Manual, 2007.

Kaewunruen, S. and Remennikov, A. M., "Dynamic effect on vibration signatures of cracks in railway prestressed concrete sleepers," *Advanced Materials Research*, 41-42, 2008, pp. 233-239.

Kaewunruen, S. and Remennikov, A. M., "Effect of a large asymmetrical wheel burden on flexural response and failure of railway concrete sleepers in track systems," *Engineering Failure Analysis*, 15, 2008, pp. 1065-1075.

Kaewunruen, S. and Remennikov, A. M., "Experimental determination of the effect of wet/dry ballast on dynamic railway sleeper/ballast interaction," *Journal of Testing and Evaluation*, 36(4), 2008, pp. 412-415.

Kaewunruen, S. and Remennikov, A. M., "Sensitivity analysis of free vibration characteristics of an in situ railway concrete sleeper to variations of rail pad parameters," *J. Sound and Vibration*, Short Communication, 298, 2006, pp.453-461.

Kaewunruen, S. and Remennikov, A. M., "Experiments into impact behaviour of railway prestressed concrete sleepers," *Engineering Failure Analysis*, 18(8), 2011, pp. 2305-2315.

Kaewunruen, S, Remennikov, AM & Aikawa, A, "A numerical study to evaluate dynamic responses of voided concrete railway sleepers to impact loading," Acoustics 2011, pp.1-8, 2011.

Lackenby, J., Indraratna, B., McDowell, G. R. and Christie, D., "Effect of confining pressure on ballast degradation and deformation under cyclic triaxial loading," *Géotechnique*, 57(6), 2007, pp. 527-536.

Leykauf, G., Mattner, L. and Steinbeißer, L., "Schwingungsmessungen mittels Schotter-Meßsteinen," *ETR- Eisenbahntechnische Rundschau*, 47(1), 1998, pp. 37-41.

Lu, M. and McDowell, G. R., "Discrete element modelling of railway ballast under triaxial conditions," *Geomechanics and Geoengineering*, 3(4), 2008, pp. 257-270.

Schmitt, L., Gautier, P.E., Sab, K., Duhamel, D. and Saussine, G., "New aspects of the dynamical effects on ballast fatigue and track settlement," *WCRR2008*, 2008, 3.4.1.1.

Shaer, A. A., Duhamel, D., Sab, K., Foret, G. and Schmitt, L., "Experimental settlement and dynamic behavior of a portion of ballasted railway track under high speed trains," *J. Sound and Vibration*, 316, 2008, pp. 211-233.

Sakai, H. and Aikawa, A., ""Three-dimensional Finite Element Analysis of Sleeper Vibration with the Influence of Ballast," *1st International Conference on Railway Technology*, Civil-Comp Press, 2012, pp. 1-15.

Stahl, W., "Untersuchung eines für HGV optimierten Schotteroberbaus, Quervershiebewiderstandsmessungen und Schwingungsverhalten," *EI-Eisenbahningenieur*, 54(5), 2003, pp.8-16.

Zhai, W. M., Wang, K. Y. and Lin, J. H., "Modelling and experiment of railway ballast vibrations," *J. Sound and Vibration*, 270(4-5), 2004, pp. 673-683.